Journal of Materials Research and Technology 36 (2025) 9881–9897

Contents lists available at ScienceDirect

Journal of Materials Research and Technology

journal homepage: www.elsevier.com/locate/jmrt

Influence of heat treatment on the high temperature properties of Inconel 718 fabricated via Laser Beam Powder Bed Fusion

P.E. May [a], M. White [b], A. Bordin [b], L. Ednie [b], R. Huff [b], S. Vunnam [c], L. Becker [c], R.J. Lancaster [a,*]

[a] Institute of Structural Materials, College of Engineering, Bay Campus, Swansea University, Swansea, SA1 8EN, United Kingdom
[b] ASTM International, USA
[c] AddUp Solution Center, 5101 Creek Rd, Cincinnati, OH, 45242, USA

ARTICLE INFO

Handling editor: L Murr

Keywords:
Additive manufacture
Dynamic strain aging
Inconel 718
Laser beam powder bed fusion

ABSTRACT

This study investigates the influence of post-manufacture heat treatments on the high-temperature performance of Inconel 718 produced via Laser Beam Powder Bed Fusion (LB-PBF). Two industrially relevant heat treatment routes were explored: one optimised for low cycle fatigue (HT1) and the other for creep resistance (HT2), and their effects were compared against as-received (AR) LB-PBF and conventionally wrought IN718. Mechanical testing, including tensile, constant load creep, and strain-controlled low cycle fatigue (LCF) at 650 °C, was complemented by extensive microstructural characterisation via EBSD, SEM, and EDX. HT1 exhibited a significantly refined microstructure, enhanced twin density, and promoted fine, well-distributed secondary phases, resulting in superior fatigue performance and creep resistance comparable to wrought material. HT2, while enhancing tensile strength and hardness relative to AR, offered limited improvement in creep resistance. All LB-PBF variants exhibited lower ductility and more heterogeneous dynamic strain aging (DSA) behaviour than the wrought alloy. The study demonstrates that tailored heat treatments can enhance the high-temperature mechanical performance of LB-PBF IN718, with HT1 identified as the most effective approach for fatigue-critical applications.

1. Introduction

Additive manufacture (AM) brings significant opportunities by offering unprecedented design freedom and the ability to produce complex geometries that are difficult or impossible to achieve with traditional methods [1,2]. Among the various AM techniques, Laser Beam Powder Bed Fusion (LB-PBF) stands out due to its precision and capability to produce high-performance parts directly from digital models. LB-PBF involves using a high-powered laser to selectively melt and fuse powdered material layer by layer, resulting in parts with high dimensional accuracy and excellent mechanical properties [3,4]. In addition to the aforementioned benefits for LB-PBF, there are many other advantages to AM such as: material efficiency, customisation and improved mechanical properties [1,5]. However, AM does have some disadvantages that need to be considered, including: inherently poor surface finish in the as-built condition, build size limitations, high initial cost, and microstructural complexities such as anisotropy and high residual stress [6]. Although there are some limitations to AM, it has been widely adopted by several industries such as aerospace [7,8], automotive [9], healthcare [10] and energy [11,12]. In order to fully integrate AM components for critical and non-critical components within these industries, the mechanical and microstructural differences between AM and their conventionally manufactured counterparts (wrought and cast) needs to be fully analysed to understand the process-structure-property-performance relationship [13–17], particularly at elevated temperatures to replicate in-service conditions.

Inconel 718 (IN718), a nickel-based superalloy, has been heavily implemented within industry because of its excellent mechanical properties, particularly at elevated temperatures of up to 650 °C [18,19]. Its unique composition provides high strength, corrosion resistance, and the ability to retain its mechanical properties in extreme environments, making it ideal for aerospace, nuclear, and industrial applications [20,21]. Consequently, IN718 has been widely adopted for use in metal AM [21–23]. The microstructure of IN718 consists of a face-centred cubic (FCC) austenitic γ matrix strengthened by secondary precipitates of gamma prime (γ′) and gamma double prime (γ‘‘) phases, which are

* Corresponding author.
E-mail address: r.j.lancaster@swansea.ac.uk (R.J. Lancaster).

https://doi.org/10.1016/j.jmrt.2025.05.140
Received 31 March 2025; Received in revised form 17 May 2025; Accepted 17 May 2025
Available online 23 May 2025

Table 1
Chemical composition of virgin IN718 powder and wrought material (wt%).

Element	C	Si	Mn	P	S	Cr	Mo	Ni
LB-PBF	0.03	0.10	0.06	<0.005	0.002	19.29	2.96	Bal.
Wrought	0.024	0.07	0.09	0.008	0.0003	17.61	2.97	Bal.
Element	**Cu**	**Co**	**Ti**	**Al**	**Nb**	**Nb (Cb) + Ta**	**B**	**Fe**
LB-PBF	0.03	0.17	1.00	0.61	5.13	5.14	0.0020	17.53
Wrought	0.06	0.35	0.95	0.53	5.12	–	0.0031	18.15
Element	**N**	**Pb**	**Ta**	**O**	**Ca**	**Mg**	**Sn**	**Se**
LB-PBF	0.011	<0.0005	0.01	0.031	0.00	0.00	–	<0.0003
Wrought	0.005	<0.0003	<0.02	<0.0003	<0.0003	0.0015	0.0012	<0.003

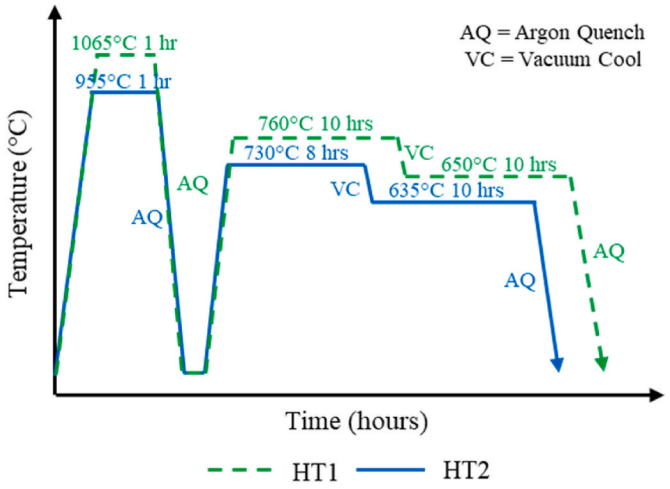

Fig. 1. Schematic of implemented heat treatments.

primarily responsible for the material's favourable high temperature properties and resistance to creep [23–25]. The γ′ phase composition of $Ni_3(Al,Ti,Nb)$ is an L12 ordered FCC phase that coherently precipitates within the matrix and hinders dislocation movement. The coherent γ'' phase has a composition of $Ni_3(Nb,Ti)$ with a body-centred tetragonal (BCT) D022 structure, which provides significant strengthening (especially at elevated temperatures) by impeding dislocation movement [26,27]. Alongside γ′ and γ'', phases such as δ, carbides, and Laves, can be present. The δ phase is an Ni_3Nb orthorhombic D0a structure that typically forms at grain boundaries and provides grain growth control during heat treatment [23]. Carbides are usually present in the form of MC, $M_{23}C_6$ or M_6C, and are found along the grain boundaries, with the primary role to enhance grain boundary strength and reduce grain boundary sliding [28]. The aforementioned phases significantly improve the mechanical properties of IN718, but on the other hand, the presence of Laves can be more detrimental. Laves are present as a hexagonal $(Ni,Fe,Cr)_2(Nb,Mo,Ti)$ structure and form during solidification and heat treatment, and are present as a brittle intermetallic phase at grain boundaries or in interdendritic regions [29]. The distribution and morphology of these phases can be controlled through heat treatment, optimising the alloy's properties for specific applications [30–33]. Franco-Correa et al. [31] showed that as-built LB-PBF IN718 displayed high concentrations of Nb-rich Laves phases, whereas wrought IN718 displayed significant amounts of δ phase. Both wrought and LB-PBF samples displayed MC carbides, but their morphology and distribution differed: in wrought, the carbides were larger (~10 μm) and located within grains, whereas in LPB-PBF material, they were smaller (~1 μm) and situated along grain boundaries. The conventional solution treatment implemented effectively dissolved δ in wrought and Laves in LB-PBF, but did not dissolve the MC carbides. Following aging heat treatment, MC carbides transformed into $M_{23}C_6$ carbides whilst forming γ'' from δ dissolution in wrought and Laves dissolution in LB-PBF. Although the variation in microstructure was seen, a similar hardness was reported in wrought and LB-PBF after applying the aging heat treatment.

The LB-PBF IN718 microstructure differs to that of its conventionally manufactured counterpart due to rapid cooling rates and thermal gradients from the AM process. LB-PBF typically exhibits a microstructure with columnar grains that align with the build direction due to epitaxial growth from partial remelting and heterogeneous nucleation, with finer grains near the build platform due to faster cooling rates and heat sink effects [34–36]. In addition, reduced cooling rates further from the platform promote micro-segregation and increased Laves phase formation [37,38]. It is also common for the microstructure of AM IN718 to present differently with varying processing parameters, influencing crystallographic texture, microstructural features and mechanical properties [39–44]. For example, Wang et al. [44] demonstrated that increasing energy density (18–1000 J/mm^3) in LB-PBF IN718 reduces lack of fusion defects, but can instead introduce keyholing at excessive levels. The optimised densities were identified between 48 and 623 J/mm^3. Overall, variations in energy density induced changes in microstructure, where high power inhibited Laves but promoted MC carbides.

Research on process parameters and heat treatments on the porosity, microstructure, and tensile properties of LB-PBF IN718 was conducted by Liu et al. [45]. The optimal route of fabrication was found to include an equivalent energy density of 60.0 J/mm^3, presenting the lowest porosity of 0.15 %, prior to heat treatment. In their study, Liu et al. adopted a regime consisting of a single solution at 980 °C for 1 h and direct aging at 720 °C for 8 h and 620 °C for 8 h. Microstructural analysis showed that in the as-built condition there was a dense network of Laves phase due to Nb and Mo segregation. This network acted as a crack initiator during tensile testing, causing reduced strength compared to heat treated samples. However, during single solution, the Laves phase dissolved and δ phase was precipitated, whereas direct aging precipitated the γ′ and γ'' phases. Also, grain size remained largely unchanged after heat treatment. Further tensile testing demonstrated that the direct aging samples exhibited the highest strength due to strain hardening and γ′ and γ'' strengthening. The single solution samples showed moderate strength but highest elongation due to the presence of δ phase along the grain boundaries [45].

Similar research conducted by Kasperovich et al. [46] also investigated optimisation of mechanical performance, via tensile testing of LB-PBF IN718 through varying process parameters and post-processing heat treatments. The optimised energy density was again found to be 60.0 J/mm^3, exhibiting a porosity volume fraction of 0.32 %. It was found that double aging at 720 °C for 8 h and 620 °C for 8 h had no effect on grain size but partially dissolved Laves and precipitated δ, γ′, and γ'' phases, compared to the as-built (AB) state. This heat treatment reduced the strength but increased ductility. For homogenisation (1155 °C for 4 h) and hot isostatic pressing (HIP) (1155 °C for 4 h at 100 MPa) the grains were enlarged, Laves and δ phases dissolved, and carbides were promoted at grain boundaries. Homogenisation displayed more γ'' phase causing higher strength and unchanged ductility but HIP

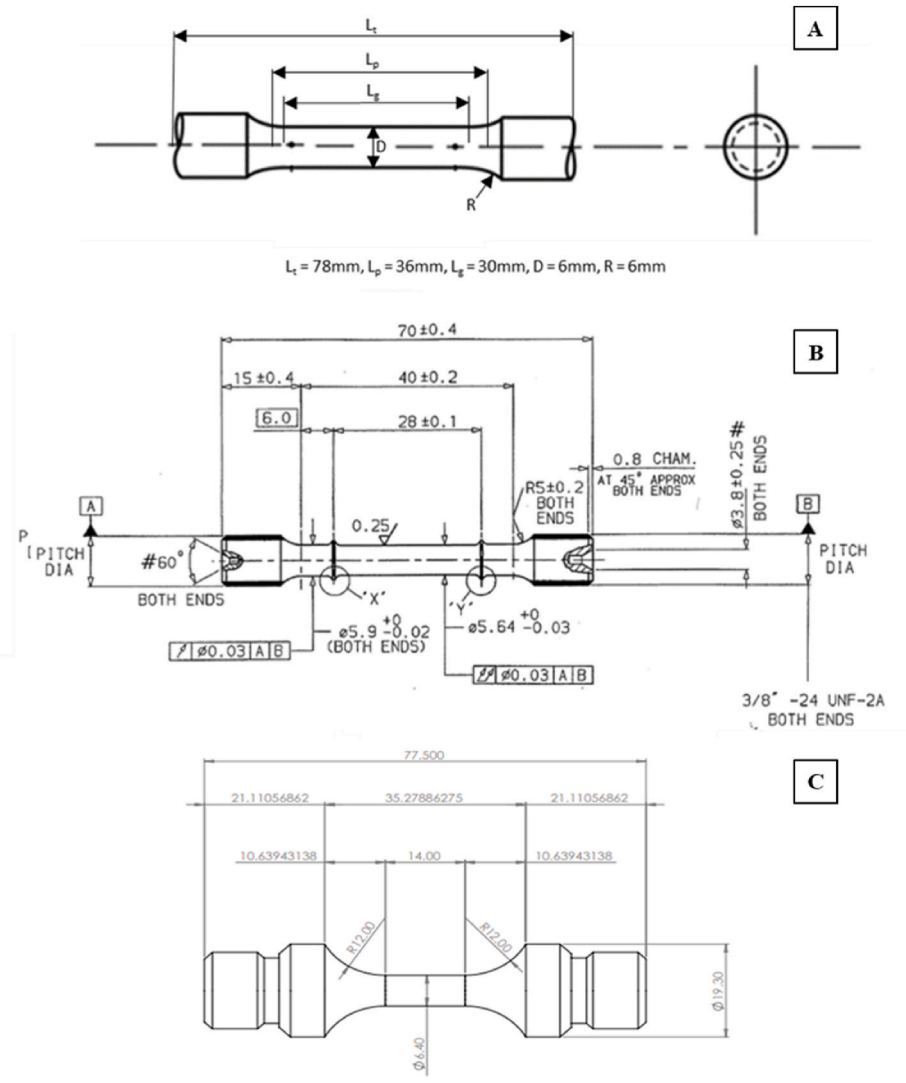

Fig. 2. Schematic diagrams of specimen dimensions of **A** tensile samples, **B** constant load creep samples and **C** low cycle fatigue samples. All dimensions in mm.

Table 2
Porosity content in wrought and LB-PBF IN718 variants.

Sample	Porosity (% area)			
	Vertical		Horizontal	
	XY	XZ	XY	XZ
As-received	0.122 ± 0.002	0.065 ± 0.003	0.099 ± 0.013	0.084 ± 0.006
Heat Treatment 1	0.118 ± 0.016	0.118 ± 0.001	0.076 ± 0.006	0.071 ± 0.021
Heat Treatment 2	0.183 ± 0.008	0.108 ± 0.002	0.097 ± 0.031	0.087 ± 0.027

maximised elongation with unchanged strength. HIP was also reported to decrease porosity from 0.32 % to 0.01 %. Combining heat treatments showed that double aging after homogenisation or HIP did not change the type of phases present but confirmed an increase in the volume of γ'' and carbide size. Double aging after HIP also showed an increase in porosity from 0.01 % to 0.03 %. Additionally, the influence of build direction was assessed, showing clear mechanical anisotropy due to texture evolution with vertically built samples exhibiting lower strength but higher ductility than horizontally built samples. The as-built and double aged samples showed the most anisotropy and reduced after homogenisation and HIP [46].

To consolidate and improve the as-built microstructure and mechanical properties of LB-PBF material, the implementation of post-processing, such as heat treatments, is essential. Consequently, this paper will investigate the influence of varying industrial heat treatment parameters on the elevated temperature (650 °C) mechanical behaviour of LB-PBF IN718. Assessment will be carried out on a wrought variant, as-received (no heat treatment) and two different heat treatments chosen to improve fatigue and creep properties, respectively. The investigation will include a through microstructural analysis and mechanical characterisation, including tensile, constant load creep and strain control low cycle fatigue (LCF) experiments.

2. Experimental

2.1. Material background

LB-PBF IN718 samples were fabricated using virgin powder produced via an inert-gas atomisation process in argon. The chemical composition is stated in Table 1. The powder size distribution (PSD) exhibited d_{10}, d_{50} and d_{90} values of 5.2 μm, 10.63 μm and 17.25 μm respectively.

Vertically (90°) built LB-PBF cylinders were fabricated on a FormUp 350 with an inert argon gas atmosphere. Parameters were set by the manufacturer to provide a volumetric energy density of 44.44 J/mm^3.

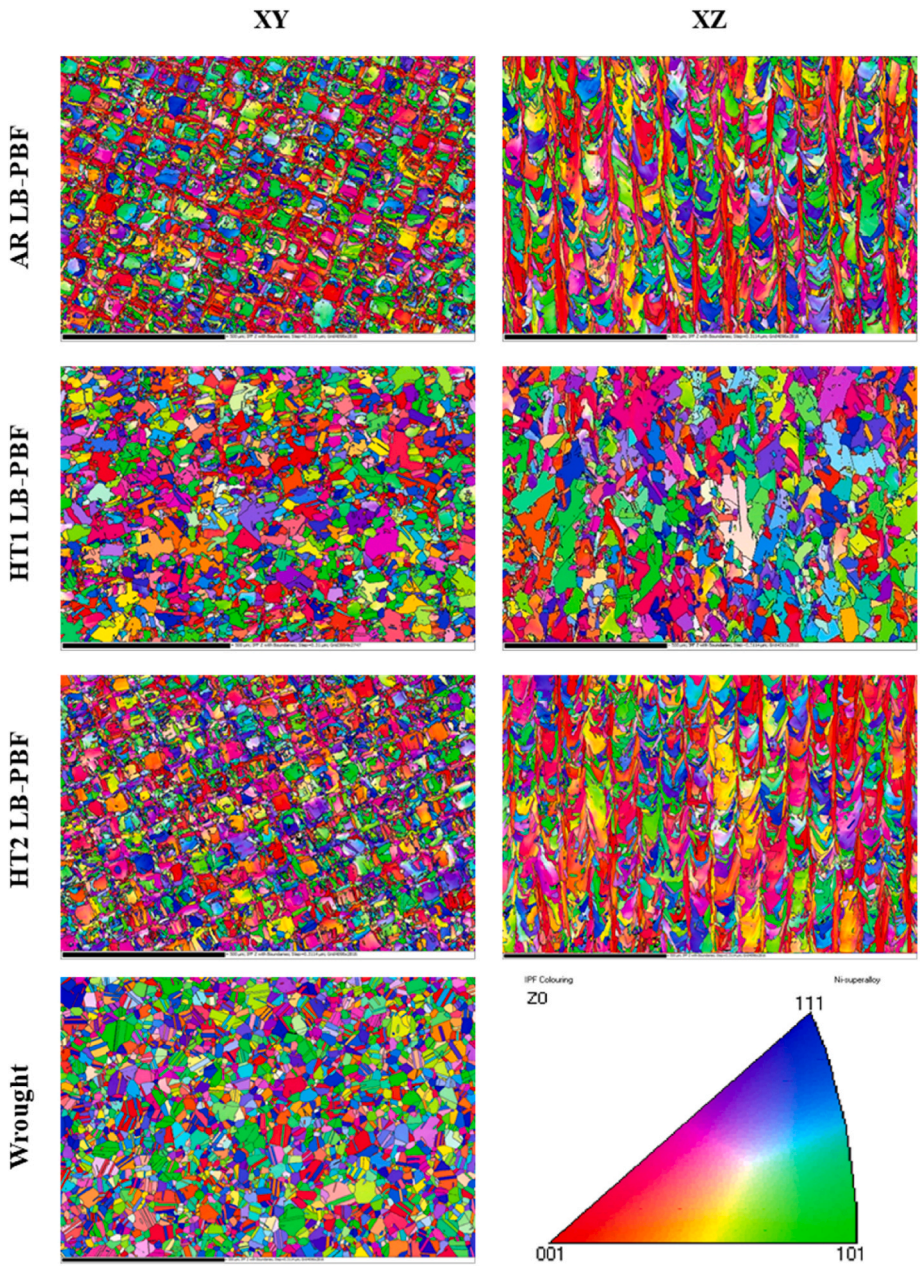

Fig. 3. EBSD maps for LB-PBF and wrought IN718.

Table 3
Grain size measurements for wrought and LB-PBF IN718 variants.

Sample ID	Without Twins			With Twins			Twin Density (%)	MUD
	Grain Area (μm^2)	Grain Diameter (μm)	Aspect Ratio	Grain Area (μm^2)	Grain Diameter (μm)	Aspect Ratio		
Wrought	618	22.5	0.67	196	12.6	0.49	51.4	1.20
AR XZ	196	10.4	0.42	195	10.4	0.42	0.5	2.27
AR XY	91	7.6	0.55	89	7.6	0.55	0.5	2.20
HT1 XZ	465	14.5	0.49	293	13.3	0.47	25.3	1.87
HT1 XY	252	11.4	0.56	166	10.4	0.52	17.6	1.60
HT2 XZ	176	9.8	0.43	174	9.8	0.43	0.3	1.53
HT2 XY	102	8.0	0.54	101	8.0	0.54	0.4	2.39

Post manufacture, the cylinders underwent various heat treatments, as detailed in Fig. 1. Heat treatment 1 (HT1) comprised of a solution anneal at 1065 °C for 1 h followed by a two-step aging treatment at 760 °C for 10 h and 650 °C for 10 h, and was designed to improve the alloy's LCF properties. Heat treatment 2 (HT2) involved a solution anneal at 955 °C for 1 h followed by a two step aging at 730 °C for 8 h and 635 °C for 10 h. HT2 was envisaged to enhance the alloy's resistance to creep damage. A selection of cylinders also remained in the as-received (AR) condition, providing three different variants of the LB-PBF material.

The behaviour of LB-PBF IN718 was also compared to the equivalent

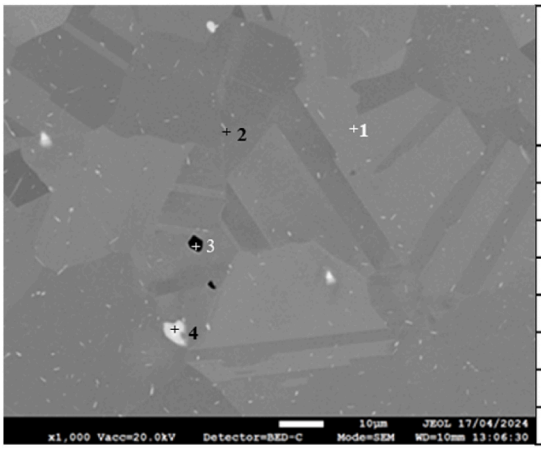

Element	Chemical Composition (wt.%)			
	Region 1 (Matrix)	Region 2 (δ)	Region 3 (TiC Carbide)	Region 4 (NbC Carbide)
Ni	48.79	51.78	1.82	1.28
Cr	19.11	11.71	1.50	0.48
Fe	16.61	10.03	0.83	0.34
C	9.23	9.30	7.04	28.76
Nb	4.52	13.09	7.18	64.18
Ti	0.88	1.63	61.37	4.96
Al	0.39	0.34	-	-
Other	Balance	Balance	Balance	Balance

Fig. 4. Unetched wrought FEG-SEM micrograph with corresponding EDS elemental analysis.

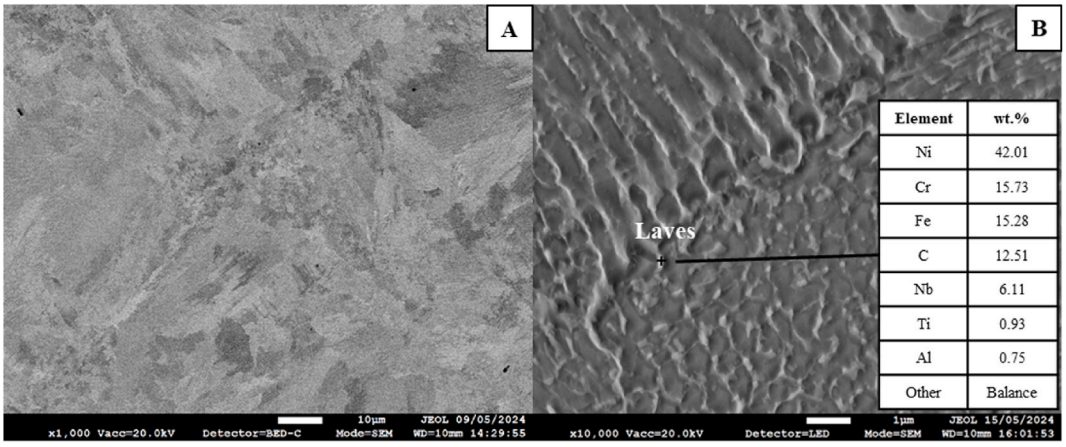

Fig. 5. **A**n unetched AR LB-PBF IN718 FEG-SEM micrograph at 1,000x magnification alongside **B** etched AR LB-PBF IN718 FEG-SEM micrograph at 10,000x magnification with EDS elemental analysis.

wrought material, that was subjected to a solution anneal treatment at 965 °C for 1 h, followed by rapid air cool. The composition of the wrought alloy is also provided in Table 1.

2.2. Microscopy

Microstructural analysis was performed using Electron Backscatter Diffraction (EBSD) on a Hitachi SU3500 Scanning Electron Microscope (SEM). Parameters for EBSD scans were consistent across all recorded maps: magnification of 100×, accelerating voltage of 20 kV, step size of 0.31 μm, and a 4x4 EBSD camera binning mode. Once captured, the EBSD scans were processed through Channel 5 Tango software where settings were defined as 10 pixel per grain minimum as per ISO 13067 [47] and critical misorientation set as greater than 10° with allowed completion to 2°. Assessment of annealing twins was also completed on Tango Channel 5 software.

Precipitate and phase analysis was assessed on a JEOL 7800F Field Emission Gun-Scanning Electron Microscope (FEG-SEM). Various methods were implemented to fully understand the precipitates present. Firstly, unetched samples were imaged to assess delta (δ) phase and carbides. The samples were then electro-etched with 10 % phosphoric acid and Kalling's No 2 to identify Laves, carbides, δ, γ′ and γ′′ phases. Electro-etching was successfully implemented by ensuring the sample was freshly polished prior to etching. Electrical settings used were 3.00 V and 0.80 mA. In addition, Energy Dispersive X-Ray Spectroscopy (EDS) was undertaken using the attached Oxford Instruments SMax 50 to understand elemental distribution.

Alongside microstructural analysis, a Hitachi SU3500 SEM was also implemented for fractographic analysis on the mechanically tested samples.

2.3. Microhardness

Vickers hardness testing was completed on a Struers Duramin-40 M3/A3/AC3 low load hardness tester with a Vickers hardness indenter. 25 indents were obtained per specimen in a 5 by 5 grid. All tests were completed to ASTM E92-17 [48] with a 1 kg load and dwell time of 10 s.

2.4. Tensile

Uniaxial tensile testing was conducted to ASTM E8/E8M [49] at 650 °C on an electromechanical screw machine. Testing was completed under strain control at 0.0003 s^{-1} (0.5 mm/min) until just after yield was reached; after this point, testing was conducted under load control conditions using a rate of 5 mm/min in order to preserve the extensometry equipment. Tensile tests were performed on samples machined in accordance to ASTM E8M, as displayed in Fig. 2a. All samples were finished with a longitudinal polish. Three elevated temperature tests were performed on each of the LB-PBF variants (AR, HT1, HT2) and the wrought material. Heat was applied using a digitally controlled furnace and was constantly monitored throughout the test by two Type N

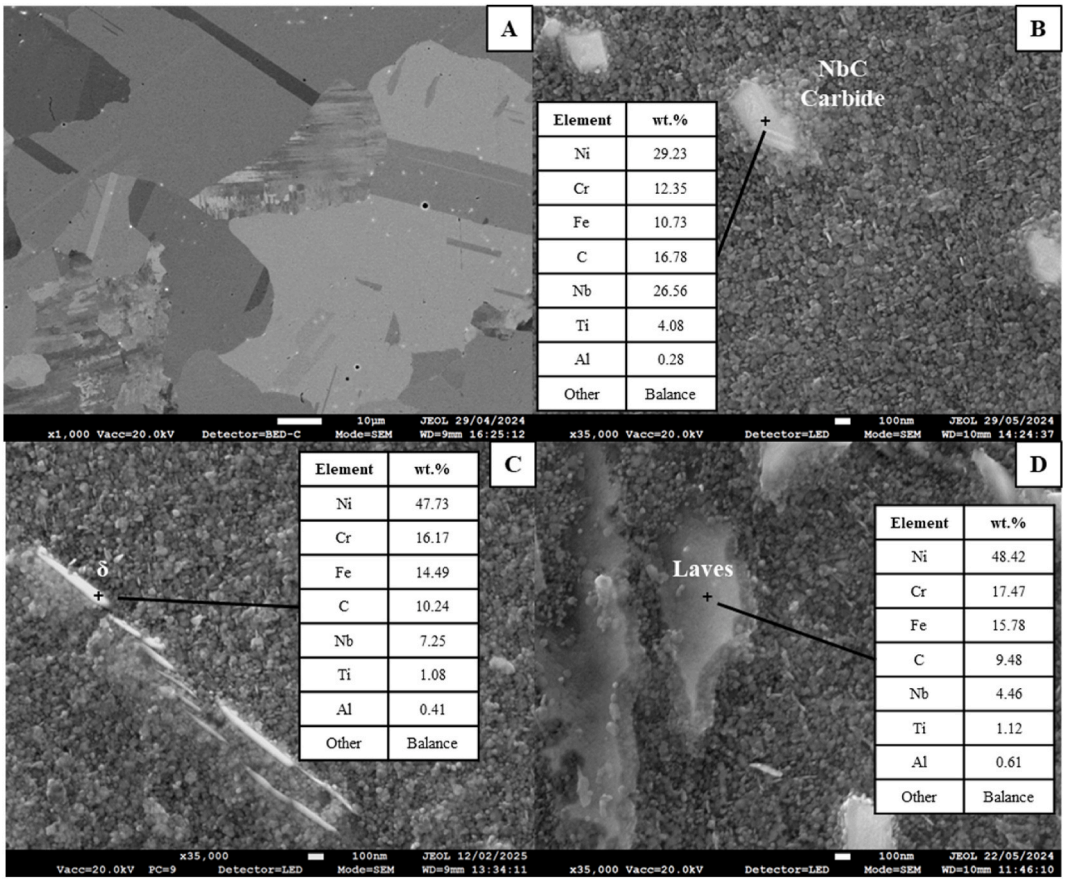

Fig. 6. **A**n unetched HT1 LB-PBF IN718 FEG-SEM micrograph at 1,000x magnification alongside **B, C** and **D** etched HT1 LB-PBF IN718 FEG-SEM micrograph at 35,000x magnification with EDS elemental analysis.

thermocouples with a tolerance of ±4 °C.

2.5. Constant load creep

Constant load creep testing was performed in accordance with ASTM E139 [50], with specimens machined to dimensions demonstrated in Fig. 2b. Samples were machined and finished with a longitudinal polish. Testing was completed on LB-PBF and wrought IN718 specimens under a temperature of 650 °C and applied loads ranging from 625 MPa to 690 MPa. Temperature was applied using a digitally controlled radiant furnace and was constantly monitored throughout the test by two Type R thermocouples with a tolerance of ±4 °C.

2.6. Strain control low cycle fatigue

Strain control low cycle fatigue (LCF) tests were completed according to ISO 12106 [51] at 650 °C on a servo-hydraulic mechanical test machine. Fatigue specimens were machined to the dimensions shown in Fig. 2c and finished with a longitudinal polish. Testing was conducted at 0.5 Hz, with a triangular waveform, and a loading R ratio of −1. Maximum strain (ε_{max}) values ranging from 0.3 % to 0.8 % were employed. The elevated temperature was applied through a standard radiant furnace and was monitored through two N type thermocouples, held within a tolerance of ±3 °C. At the end of each LCF test, the number of fatigue cycles to failure, N_f, was defined as the point at which there was a 50 % drop of the maximum peak stress from the stabilised (N_f/2) condition.

3. Results and discussion

3.1. Material and microstructure

Prior to microstructural investigation, a defect analysis was undertaken on each of the AM materials. In each variant, three separate sections of material were analysed on both the XY and XZ planes, where three separate images were recorded on each. Porosity values were recorded on each image using ImageJ software, from which average porosity values were calculated for each material type, as displayed in Table 2. As shown, all samples were deemed to be fully dense (>99.8 %).

The microstructure of LB-PBF and wrought IN718 are presented in Fig. 3. For the LB-PBF materials, both the XY and XZ planes are shown to illustrate the anisotropy present in the microstructure. Whereas for wrought IN718, only the XY plane is shown as the material is isotropic. In each of the LB-PBF samples, there is no significant texture present in the epitaxial <100> orientation as multiple of uniform density (MUD) values all fell below 3.0, yet each of the materials can be seen to have a level of anisotropy, as demonstrated by the long, columnar grains exhibited in the XZ plane and smaller, equiaxed grains on the orthogonal XY plane. Overall, the LB-PBF materials appear finer than the large equiaxed grains exhibited by the wrought material. In each material variant, grain size measurements such as grain area, grain diameter and aspect ratio, were all calculated based on elliptical fittings, with each of the respective values presented in Table 3.

It is also prevalent that the wrought material contains more evidence of twinning than the LB-PBF material. As shown, values are reported both with and without twins included. It is clear that the AR and HT1 variants exhibit a similar microstructure, with refined equiaxed grains observed in the XY plane and long, columnar grains in the XZ plane. In

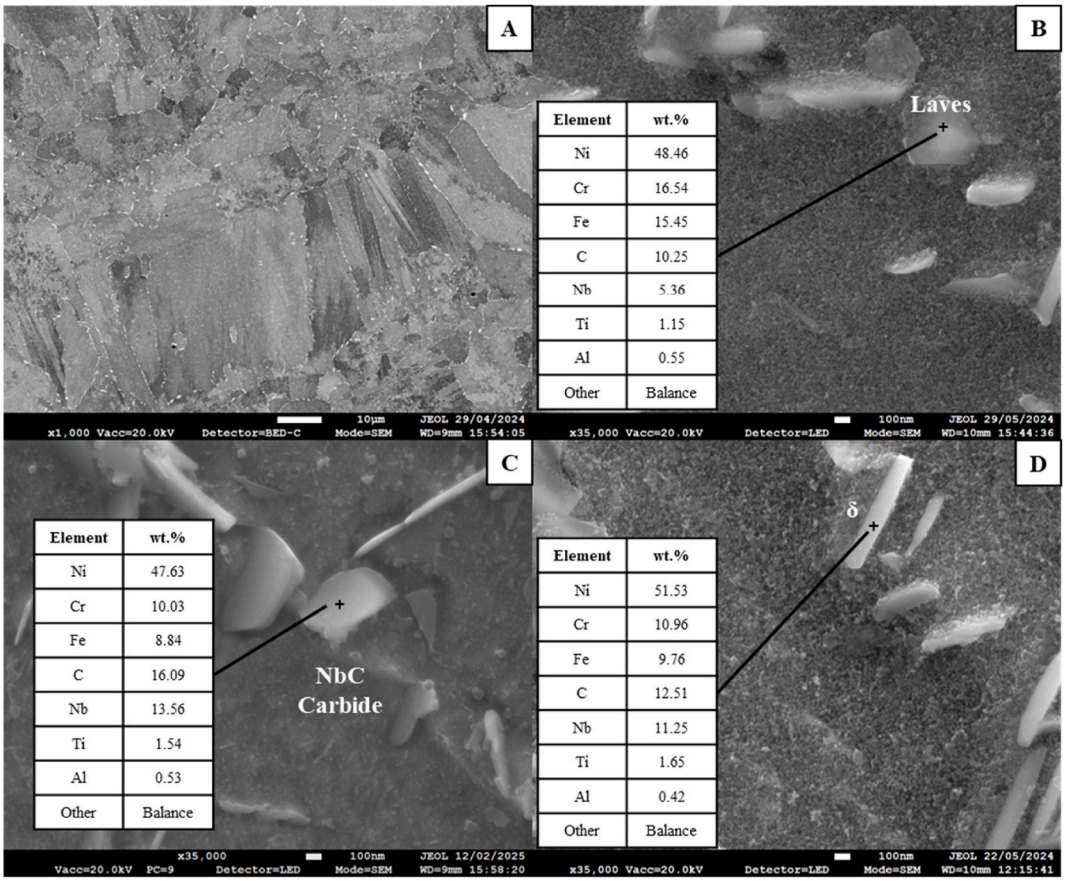

Fig. 7. An unetched HT2 LB-PBF IN718 FEG-SEM micrograph at 1,000x magnification alongside **B, C** and **D** etched HT2 LB-PBF IN718 FEG-SEM micrograph at 35,000x magnification with EDS elemental analysis.

Table 4
Vickers microhardness results for wrought and LB-PBF IN718 material variants.

Sample	Hardness (HV/1)	
	XY	XZ
Wrought	213 ± 6	222 ± 6
As-received	326 ± 5	333 ± 8
Heat Treatment 1	469 ± 14	475 ± 8
Heat Treatment 2	480 ± 11	485 ± 12

comparison, HT2 shows larger grains in both the XZ and XY planes, respectively. Although there is an increase in grain size, there is indication of anisotropy still present due to the difference in grain area, grain diameter, and aspect ratio, between the two orthogonal planes. Overall, the wrought sample has the largest grain area, grain diameter and aspect ratio (when twins are not included). Out of the LB-PBF samples, HT1 presents the highest twin density (AR = 0.5 %, HT1 = 21.5 %, HT2 = 0.35 %), but this is still significantly lower than the wrought material, which exhibited a twin density percentage of 51.4 %.

Further microstructural analysis was undertaken on a FEG-SEM and EDS to produce micrographs and compositions to identify and analyse the different phases (carbides, laves, δ, γ′, γ′′) present within the various IN718 samples. Wrought, AR, HT1 and HT2 micrographs are shown in Figs. 4–7 respectively, with supporting EDS data included within the respective figures. The wrought variant exhibits large blocky carbides (as highlighted by feature number 4, Fig. 4) with finely dispersed δ phase (feature 2), which can be seen to be significantly different to the phase morphology and quantity present across the LB-PBF samples. AR LB-PBF IN718 shows a large continuous Laves network present within the γ matrix (as shown in Fig. 5). In contrast, as given in Fig. 6, HT1

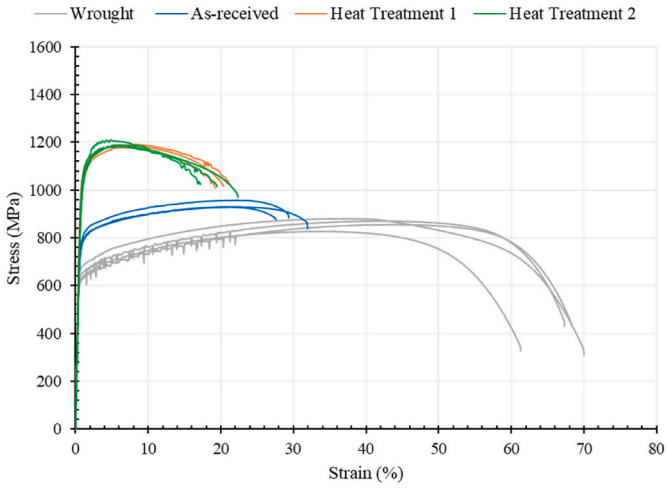

Fig. 8. Stress-strain curves of wrought and LB-PBF IN718 material variants generated at 650 °C.

presents a γ matrix with fine, dispersed carbides (Fig. 6b), δ (Fig. 6c) and Laves (Fig. 6d) phases across grains and grain boundaries. At higher magnification the presence of γ′ and γ′′ is noticeable, which is not the case for wrought and AR LB-PBF IN718. In addition, the effect of HT2 on LB-PBF IN718 can be seen in Fig. 7 with the high presence of Laves (Fig. 7b), carbides (Fig. 7c) and δ (Fig. 7d) predominantly located at grain boundaries. Similarly to HT2, at higher magnifications, the presence of γ′ and γ′′ can be observed. Although EDS cannot be implemented

Table 5
Tensile properties for wrought and LB-PBF IN718 material variants generated at 650 °C.

Sample	UTS (MPa)	0.2 PS (MPa)	YS (MPa)	Strain to Failure (%)
Wrought	858 ± 19.9	632 ± 21.9	629 ± 14.6	66 ± 3.3
AR	938 ± 13.1	759 ± 14.1	726 ± 5.1	29 ± 1.7
HT1	1186 ± 5.7	1034 ± 6.5	968 ± 16.1	20 ± 0.8
HT2	1193 ± 11.7	1012 ± 13.8	911 ± 14.4	19 ± 2.1

to determine γ′ and γ‘‘, the morphology (circular for γ′ and disc-like for γ’’) aligns with previous research [52–55].

3.2. Microhardness

Results from Vickers microhardness testing are presented in Table 4. The microhardness trends exhibited by the different sample types can be directly linked to the respective underlying microstructures. The low hardness values exhibited in the wrought material are linked to their large grain size when compared to the LB-PBF samples. A larger grain size means fewer grain boundaries, therefore, less ‘resistance’ when indenting causing a lower hardness value. Consequently, the more refined grain size, as presented by the LB-PBF samples, is reflected by an increased hardness value. For AR, HT1, and HT2, the different phase types, quantity, and location, contributes to the variation in hardness between the different AM samples. The presence of carbides and δ is linked to the higher hardness seen in the heat treated samples (HT1, HT2) compared to the non-heat treated sample (AR). Although HT1 and HT2 appear to display similar hardness averages, there is a slight increase for HT2, which is likely due to the increased quantity of carbides and δ situated along grain boundaries. The increased quantity and location influences the material’s ability to resist pile-up and deformation, hence the increased hardness in HT2.

3.3. Tensile

A series of tensile tests were performed on the various IN718 materials at elevated temperature. Fig. 8 present the stress-strain curves derived from the tests performed at 650 °C. The mechanical property data generated from the experiments are displayed in Table 5. The results show that the LB-PBF samples exhibit a higher ultimate tensile strength (UTS), 0.2 % proof stress (PS), and yield stress (YS), but reduced strain to failure when compared to the wrought material. Despite the alternative HT regimes, HT1 and HT2 samples exhibit a very similar behaviour across all property measures, far exceeding the strength based properties of the AR equivalent.

The behaviours of the IN718 variants are closely tied to their microstructural morphologies. While the grain sizes in the LB-PBF materials are very similar, showing minimal variation across all four material properties, the wrought variant exhibits a significantly larger average grain size to that of the LB-PBF samples. Consequently, the reduced grain boundary area in the wrought alloy leads to a notable

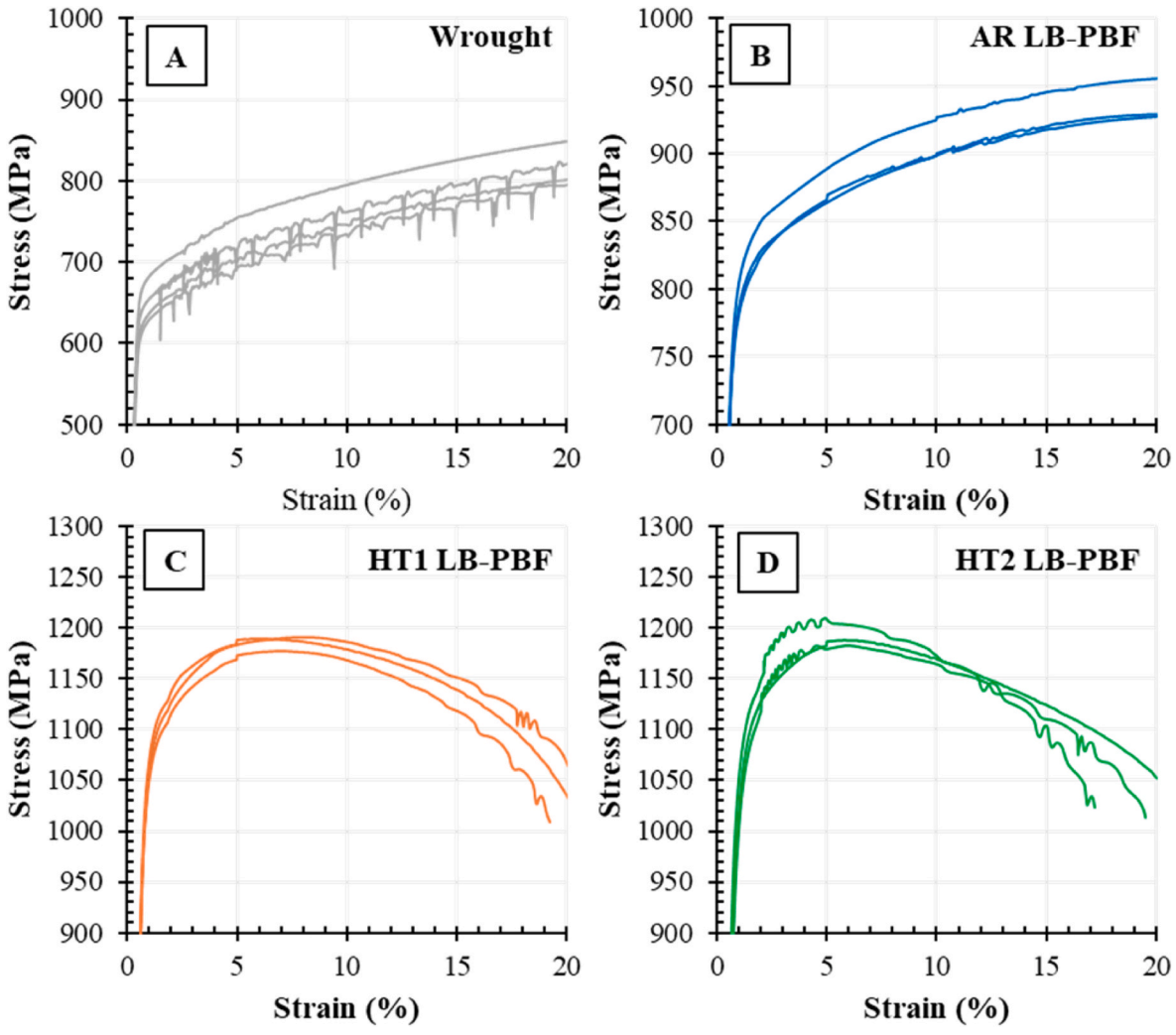

Fig. 9. Stress-strain curves of wrought and LB-PBF IN718 material variants generated at 650 °C, highlighting serrated yield resulting from dynamic strain aging.

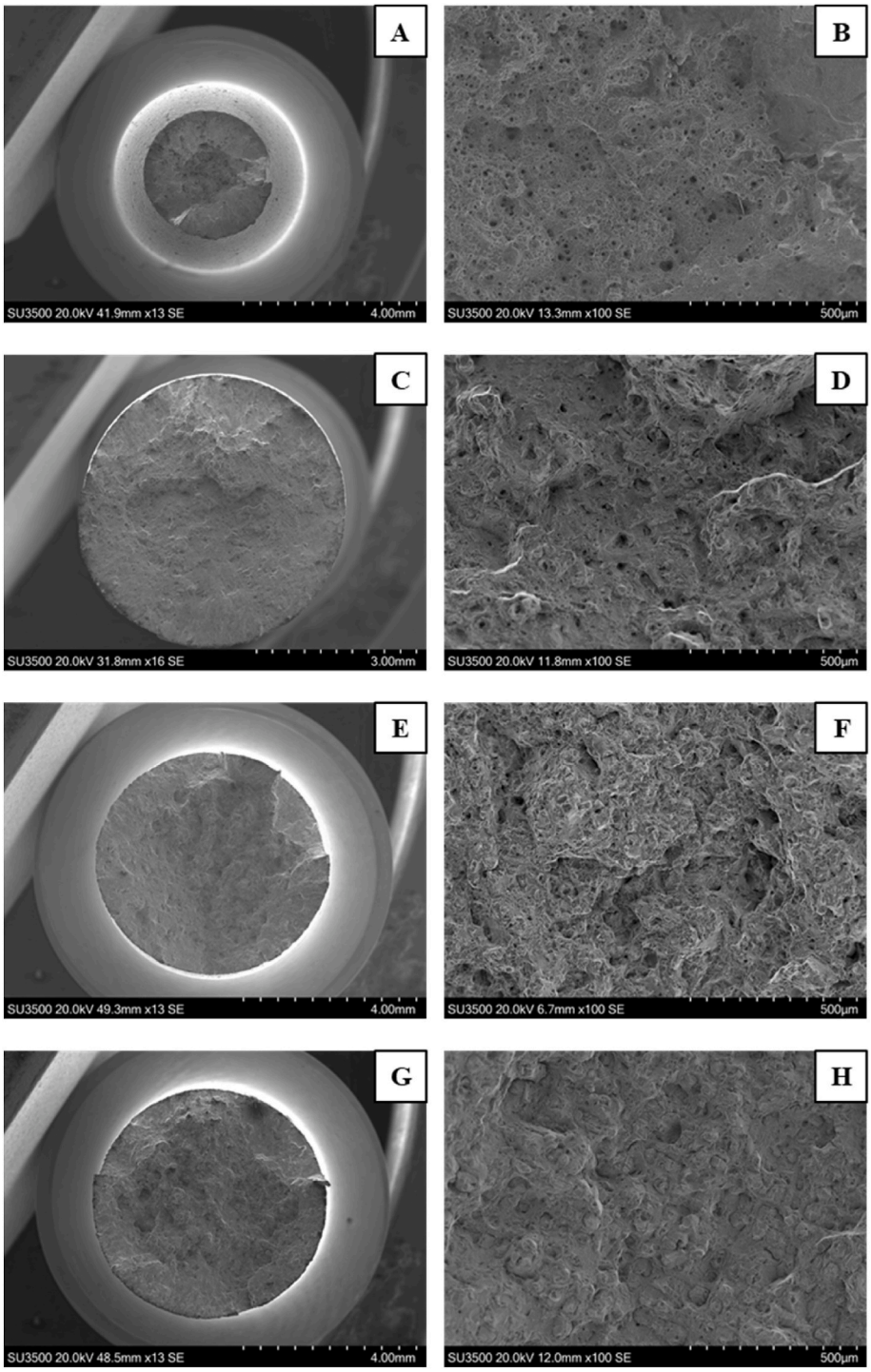

Fig. 10. SEM fractographic images of wrought and LB-PBF IN718 tensile samples at low magnification (left column) and higher magnification (right column). **A** and **B** are wrought. **C** and **D** are AR. **E** and **F** are HT1. **G** and **H** are HT2.

decrease in tensile properties compared to the LPBF samples, but with far superior ductility. Despite this, it is also important to consider the role of secondary strengthening phases. As shown in Figs. 4–7, the LB-PBF HT samples appear to exhibit a much higher volume fraction of δ and γ'' phases compared to the wrought and AR materials [54]. Furthermore, even though the presence of γ′ is less dominant than γ'' in IN718, γ' can provide additional strengthening at elevated temperatures. Likewise, the increased δ volume fraction in the HT variants can aid in grain boundary pinning, which subsequently refines the microstructure. However, excess δ can also be detrimental, having an adverse effect on ductility, as seen previously [56] and shown in Fig. 8. Therefore, a combination of these microstructural differences have contributed to the superior tensile performance observed in the LB-PBF HT materials compared to the wrought alloy.

Another notable feature is the presence of dynamic strain aging (DSA) at 650 °C. DSA represents an instability in plastic flow, associated with interactions between moving dislocations and diffusing solute atoms that can lead to increased strength, reduced ductility, and sometimes serrated flow in stress-strain curves, as seen in Fig. 9. DSA appears to be present in all the tensile curves for the different material

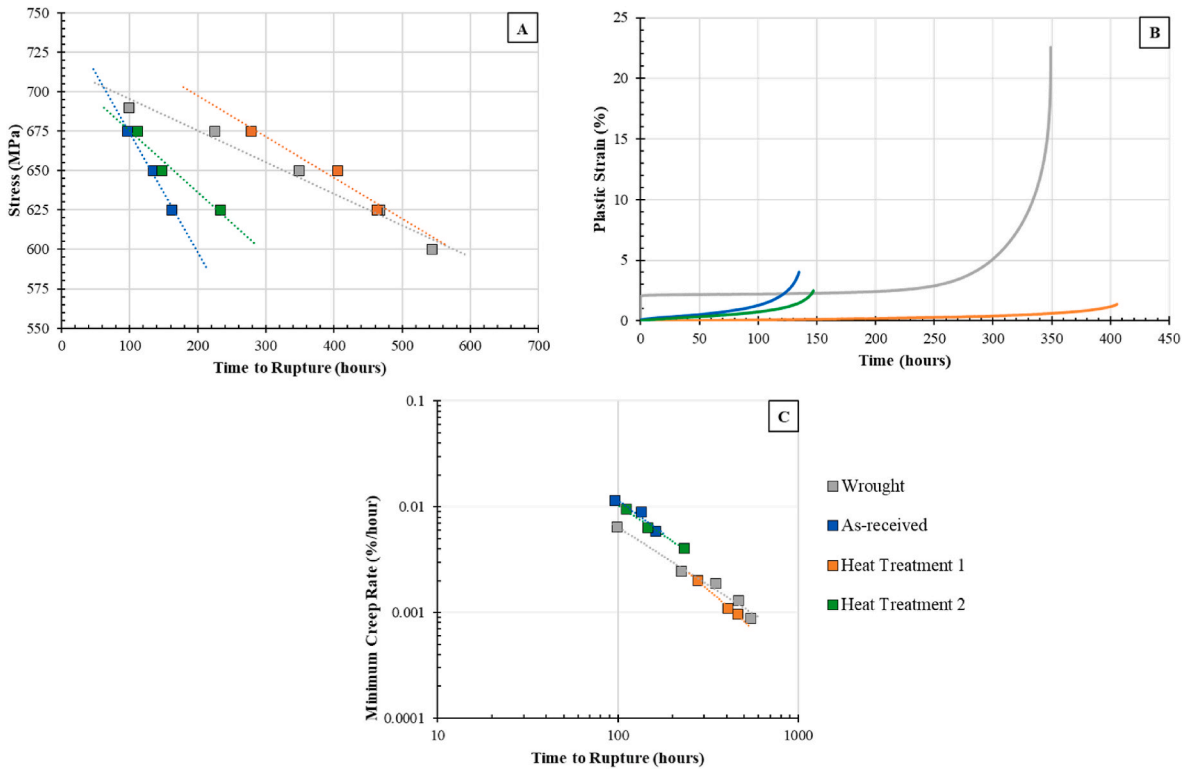

Fig. 11. Creep behaviour of wrought and LB-PBF IN718 variants tested under constant load creep conditions at 650 °C and LB-PBF IN718 variants tested under constant load creep conditions at 650 °C **A** Stress - Time to Rupture behaviour, **B** Strain - Time plots and **C** Monkman-Grant relationship.

variants, yet the type of DSA and magnitude differs. As shown, the wrought material exhibits the most significant DSA, predominantly types B and C, whereas the LB-PBF variants show less prominent DSA, associated more with types D and E. Generally, types B–C occur at elevated temperature and consist of continuous or sharp drops in stress followed by gradual recovery, indicating a strong interaction and pinning behaviour between the dislocations and diffusing solute atoms. Types D and E are far less common, and are characterised by irregular fluctuations in the stress-strain curve and typically represent a transitional behaviour between other serration types.

DSA in IN718 is particularly prevalent at elevated temperatures between 300 and 700 °C, and γ′ and γ′′ strengthening precipitates can also influence the extent of this serrated yield behaviour. Rezende et al. [57] found that in IN718 in the solution-treated condition, the serrated yielding associated with DSA is prominent across a wide temperature range (125 °C–625 °C), with the type of serration varying based on the specific temperature and strain rate. Yet, in the aged condition, the presence of precipitates, such as γ′′ and δ phases, can suppress or modify serration behaviour by hindering dislocation movement.

Such phenomena can consequently affect the mechanical behaviour, such as increased work hardening and reduced ductility [58]. This is particularly evident in the LB-PBF HT variants, which experience the largest magnitude of work hardening amongst the various IN718 materials, and also the greatest reduction in elongation. This is attributed to the increased presence of secondary strengthening precipitates in the HT materials, resulting from the aging period during the respective heat treatments. However, Weaver et al. [59] previously found that a longer annealing treatment for 110 h at 750 °C can actually result in the disappearance of DSA in IN718, as a result of solute depletion due to precipitation.

The consistency of the DSA present within the different IN718 samples also reflects the homogeneity of the microstructure. Wrought displays consistent, regular, repeating, serrations whereas the LB-PBF variants are more sporadic and irregular. This is likely due to the homogenous microstructure presented by wrought and the more heterogenous microstructure presented by the LB-PBF variants.

SEM fractographic images are presented in Fig. 10. From Fig. 10 it is clear that the wrought samples are the most ductile, with clear evidence of necking (and a reduced cross-sectional area), a high presence of dimpling and micro-voids and pronounced shear lips on the fracture surface. The LB-PBF samples also show some evidence of ductility due to the presence of micro-voids, but the presence of ductile features is far less abundant than what is seen in the wrought samples.

3.4. Constant load creep

Results from constant load creep testing, presented in Fig. 11a, shows the rupture life of the wrought and LB-PBF IN718 samples at varying stresses at 650 °C. Trends from Fig. 11a suggest that wrought and HT1 are the superior material types when considering creep resistance, whilst the AR and HT2 variants appear similar in performance yet inferior to the other materials. The creep behaviours of the different samples can be linked to their respective grain sizes and microstructural constituents. Despite the wrought and HT1 materials offering a similar level of creep resistance, the underlying reasons for this differ. The wrought material exhibits the largest grain size (618 μm^2), followed by the HT1 material (465 μm^2) on the XZ plane, and finally the AR and HT2 variants, which are very similar in morphology. However, despite this considerable difference in grain size, the HT1 material benefits from the presence of grain boundary strengthening phases in the form of fine, dispersed carbides and δ phase located in both intra- and intergranular locations (Fig. 6). In IN718, grain boundary Nb based carbides and δ phase can typically enhance creep resistance by precipitating along grain boundaries, acting as obstacles to dislocation movement and impeding grain boundary sliding. However, Gao et al. [60] reported that after prolonged exposure at elevated temperatures, Nb carbides can interact with environmental elements, such as oxygen, leading to the formation of brittle niobium oxides (e.g. Nb_2O_5) at grain boundaries.

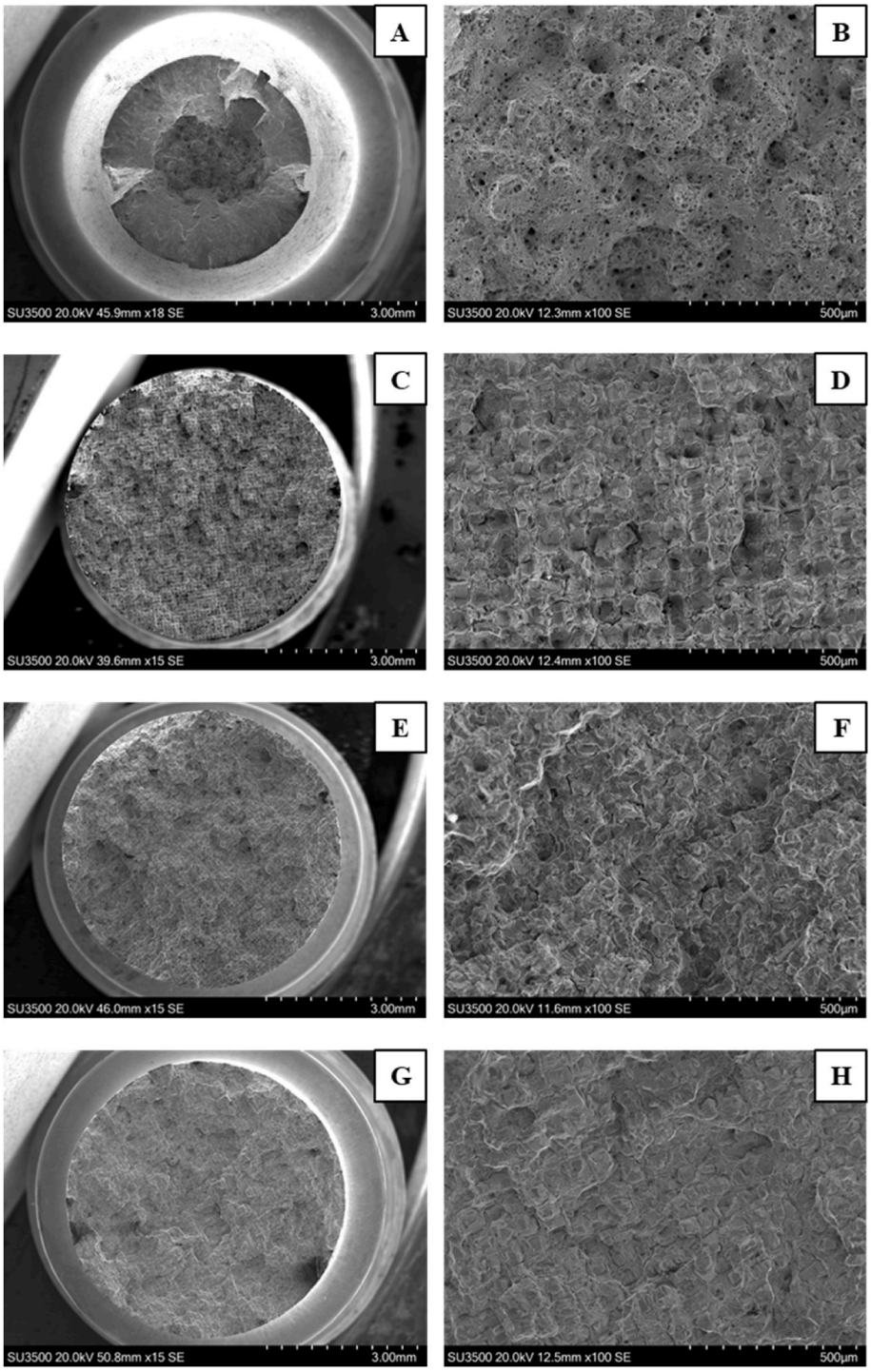

Fig. 12. SEM fractography images of wrought and LB-PBF IN718 creep samples at low magnification (left column) and higher magnification (right column). **A** and **B** are wrought. **C** and **D** are AR. **E** and **F** are HT1. **G** and **H** are HT2.

The oxides can then facilitate crack initiation and propagation, thereby reducing creep life. Therefore, it can be suggested that at lower applied stress levels where creep lives would be expected to be longer, the wrought material would be envisaged to outperform the HT1 variant due to the expected increase in brittle oxides in the heat treated material. This can be seen when comparing the trendlines in Fig. 11a.

A direct comparison of the creep deformation curves for each of the IN718 variants is presented in Fig. 11b. Here, all tests were performed under the same conditions (650 MPa and 650 °C). As expected, the wrought and HT1 materials exhibit a slower minimum creep rate during secondary stage creep, and therefore, a longer rupture life compared to AR and HT2. This is further supported by Fig. 11c, where minimum creep rate of all samples tested is presented. Again, two distinct behaviours can be observed, with the wrought and HT1 materials clearly outperforming the AR and HT2 variants. This suggests that wrought and HT1 have a lower minimum creep rate compared to AR and HT2.

The superior ductility based properties of the wrought material (previously detailed in Fig. 8) are again evidenced in Fig. 11b. The wrought material experiences a significantly higher volume of plastic strain prior to rupture than the LB-PBF equivalents. This behaviour is

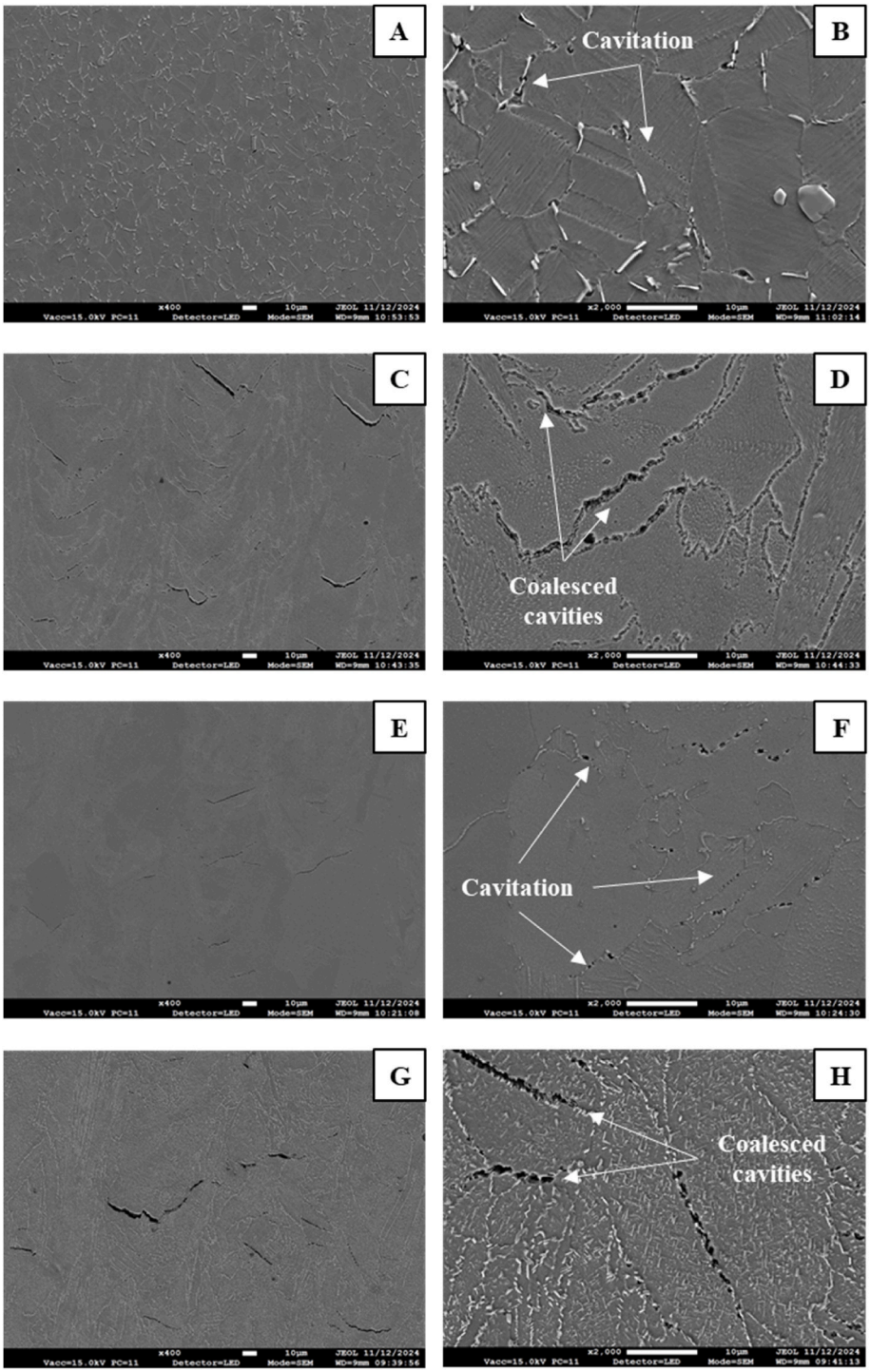

Fig. 13. FEG-SEM micrographs of wrought and LB-PBF IN718 creep samples at lower magnification (left column) and higher magnification (right column). **A** and **B** are wrought. **C** and **D** are AR. **E** and **F** are HT1. **G** and **H** are HT2.

linked to the larger grain size of the material, where dislocations can move more freely through the crystal lattice, allowing the material to deform plastically without fracturing. This can enhance ductility, especially at higher temperatures where dislocation glide and climb are more active. Furthermore, the greater twin percentage in the wrought variant will also favour the material's creep behaviour as twins help accommodate plastic strain and delay failure by redistributing stress in the material. However, excessive twinning can also accelerate failure in the tertiary creep stage.

Zhang et al. [61] found that in selective laser melted (SLM) IN718, during the steady-state creep stage, only a few slip systems are activated within individual grains, which typically exhibit an irregular grain morphology. However, in contrast, most slip systems in the forged variant of IN718 contain a regular grain morphology, where slip can be activated leading to greater ductility. Furthermore, the authors found that the primary deformation mechanism in SLM IN718 during the steady-state secondary creep stage was micro-twinning, whereas in the forged material, both dislocation slip and micro-twinning contributed to deformation during secondary creep [61].

Post-test analysis was conducted to assess the fracture surfaces and

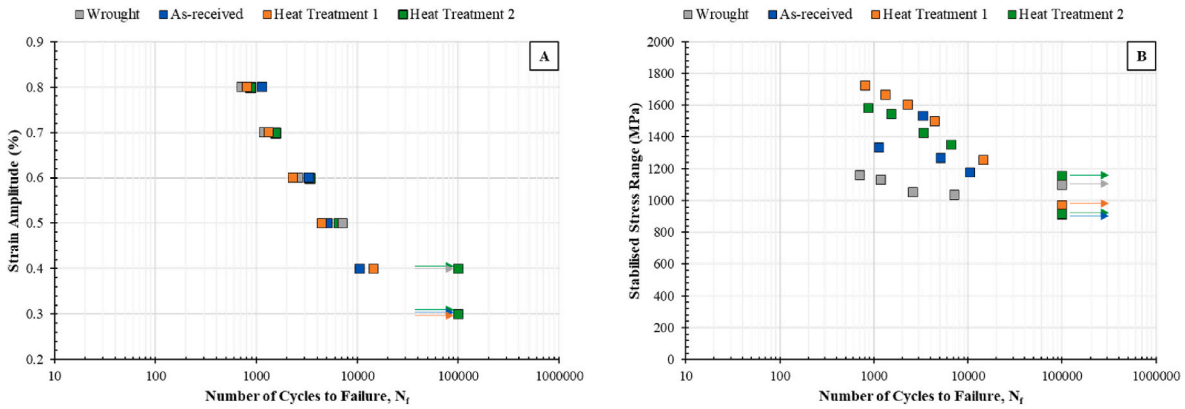

Fig. 14. LCF behaviour for wrought and LB-PBF IN718 at 650 °C, **A** Strain amplitude and **B** Stabilised stress range.

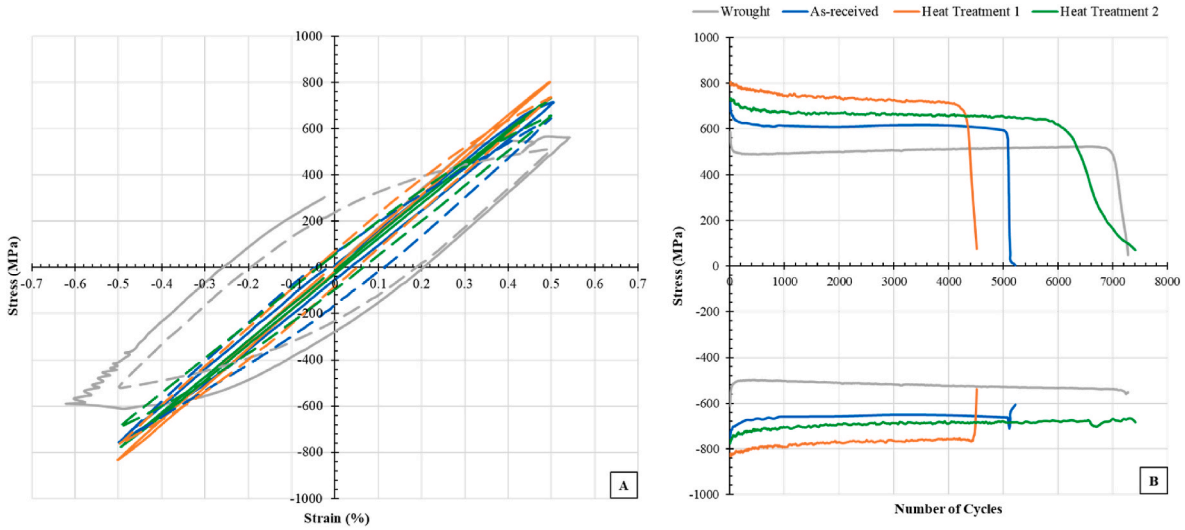

Fig. 15. LCF behaviour of wrought and LB-PBF IN718 at 0.5 % strain amplitude and 650 °C **A** monotonic (solid) and stabilised hysteresis (dashed) loops and **B** mmaximum and minimum stress against number of cycles.

the cavitation behaviour within the microstructures of the respective materials. Fractographic images are shown in Fig. 12. These show that the wrought material exhibits the most ductility with a more prominent presence of micro-voids (Fig. 12b) compared to the LB-PBF materials, all of which failed in a predominantly brittle nature in a somewhat checkerboard pattern. Kuo et al. [62] previously reported similar findings when investigating the creep behaviour of SLM IN718. In their paper, the authors considered the higher cooling rate in the SLM process which led to an increased dislocation density and the formation of inter-dendritic precipitates, resulting in inferior creep properties in SLM alloys. More recently, Oros et al. [63] directly compared the creep properties of LB-PBF and forged IN718 at 650 °C. They found that the AM alloy exhibited higher creep strength than the wrought alloy across nearly all applied stress levels (488–819 MPa), and attributed this to the increased volume fractions of γ" in the matrix and carbides at grain boundaries. However, like that found in this study, the creep rupture ductility properties were significantly lower in the AM material compared to the forged equivalent [63].

Following fractographic analysis, samples were sectioned in the XZ plane and cavitation analysis was completed on a FEG-SEM, as shown in Fig. 13. From this it can be seen that wrought and HT1 materials show cavitations that are uncoalesced whereas AR and HT2 show more severe cavities that have coalesced. The presence of coalesced cavities indicates a faster creep rate, a shorter period of tertiary creep and a shorter time to rupture, which directly reflects the data seen in Fig. 11. Zhang et al. [61] previously reported on the reduced tertiary creep stage in SLM IN718. They found that during the tertiary creep stage, the irregular grain morphology of SLM IN718 resulted in more severe stress concentrations developing at the grain boundaries in the form of triple point cracks, and a subsequently reduced creep performance [61].

3.5. Strain control low cycle fatigue

A series of strain controlled low cycle fatigue tests were performed on the various IN718 materials, with the results presented in Fig. 14a (strain amplitude) and Fig. 14b (stabilised stress range). Assessment of the strain amplitude data shows that the different variants generally behave very similarly, with minimal scatter observed across the material types, particularly at higher strain levels. However, when the same results are compared under their stabilised stress range response (Fig. 14b), a more clearer trend is established. The results indicate a more distinct ordering of the materials, where HT1 generally offers the best LCF performance, followed by HT2, AR and finally the wrought variant.

Sonntag et al. [64] recently undertook a similar study, comparing the LCF behaviour of wrought and LB-PBF IN718 materials. In their study, the LB-PBF material was subjected to a post manufacture HT, similar to HT1 in this paper. In both studies, a stress relief/homogenisation treatment was performed at 1065 °C for 1–1.5 h, followed by air cooling to 50 °C. Then in this research, the material was reheated to 765 °C for

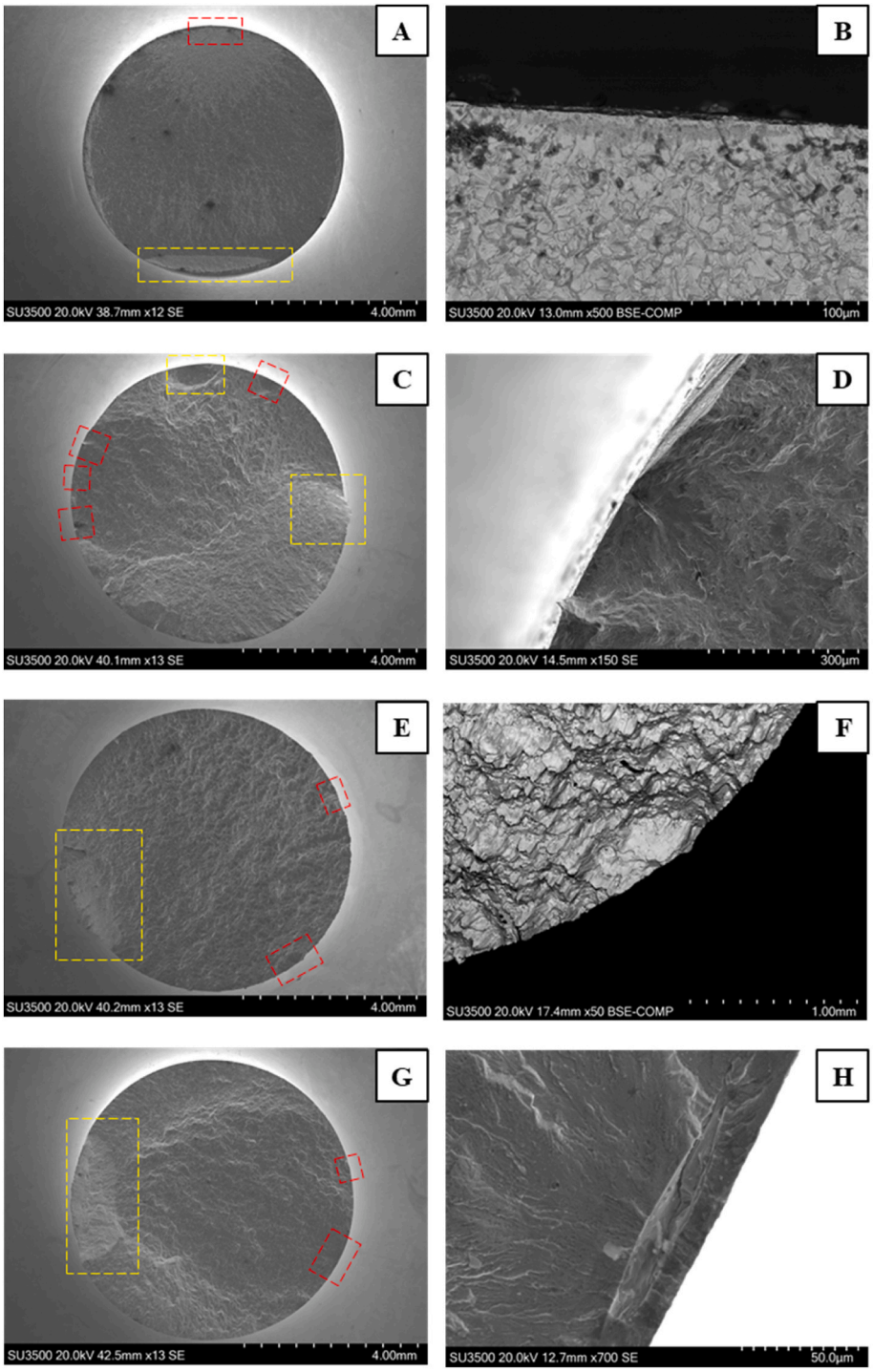

Fig. 16. SEM fractographic images of wrought and LB-PBF IN718 LCF samples tested at 0.5 % and 650 °C, at low magnification (left column) and higher magnification (right column). **A** and **B** are wrought. **C** and **D** are AR. **E** and **F** are HT1. **G** and **H** are HT2.

10 h for solution treating, vacuum cooled to 650 °C for 10 h for ageing and finally argon quenched. In contrast, Sonntag et al. solution treated at a higher temperature of 965 °C for 1 h, air cooled to 50 °C, followed by a two-stage aging treatment at 720 °C for 8 h and 620 °C for 8 h prior to air cooling. In their research, a total of three strain controlled LCF results were generated on the wrought and LB-PBF material, at a temperature of 650 °C and R = −1. On analysing the LCF results, the data generated in this paper appear to slightly outperform those presented by Sonntag et al., where across comparable applied strain amplitudes (0.5 and 0.7 %), both the wrought and LB-PBF materials exhibit slightly longer fatigue lives. Yet across both studies, LB-PBF IN718 outperforms the wrought equivalent.

Focussing on the 0.5 % strain amplitude tests, the monotonic and stabilised hysteresis loops for the different samples can be seen in Fig. 15a. Assessment of the data shows that the wrought material exhibits a considerably greater amount of plasticity on the first cycle compared to the LB-PBF samples, with HT1 and HT2 showing the least, staying predominantly within the elastic region until reaching the stabilised condition. All variants undergo cyclic softening. Additionally, the first loop of the wrought material shows stress drops near the peak stress

and an exceedance of the defined 0.5 % strain amplitude (which was corrected within subsequent cycles). This behaviour has been attributed to DSA and the extensometry attempting to correct itself.

The corresponding maximum and minimum stress recordings for the 0.5 % strain amplitude tests are shown in Fig. 15b. All the material variants appear to cyclically soften almost immediately, but the softening is generally less pronounced in the LB-PBF variants compared to the wrought material. Of the LB-PBF materials, HT1 can be seen to maintain a higher level of stress throughout the duration of the test, indicating that the HT has been beneficial to the fatigue properties.

Sonntag et al. [64], observed a similar behaviour when assessing the LCF behaviour of wrought and LB-PBF IN718 at 650 °C. In their study, the fatigue lives of the LB-PBF variant were slightly higher than those of the forged material, and the slower rate of softening observed in the LB-PBF material may contribute to this slight increase in fatigue life.

As shown earlier, the microstructure of LB-PBF IN718 is characterised by features such as Laves and δ phases, which play a pivotal role in the material's fatigue performance. At elevated temperatures, these brittle phases can precipitate along grain boundaries, leading to grain boundary embrittlement and providing pathways for crack propagation [65]. Therefore, despite the LB-PBF variants achieving higher stresses through the initial strengthening provided by the precipitation of Laves phase, after prolonged exposure, these features have a negative impact and can act as potential crack initiation sites and sources for accelerated crack propagation.

In a similar study, Nezhadfar et al. [66] investigated the high temperature fatigue behaviour and microstructural evolution of IN718 produced by laser beam directed energy deposition (LB-DED). In their research, they analysed the critical role of post-processing heat treatments in enhancing fatigue resistance and found that eliminating detrimental phases such as Laves and promoting the precipitation of strengthening phases like γ' and γ'' through tailored heat treatments, can significantly improve fatigue life. Among the heat treatments evaluated, a homogenisation process at 1065 °C for 1 h followed by aging yielded the best fatigue performance, attributed to the formation of needle-like δ phases that mitigated the adverse effects of pores. Whilst porosity was not evidenced in the current research, the presence of δ has enhanced the LCF properties of the LB-PBF material, yet the presence of Laves has led to an embrittling behaviour.

Post-test fractographic analysis was conducted on the 0.5 % strain amplitude LCF samples. An overall, low magnification image was captured for each sample, as shown in Fig. 16A, C, E and G. All the fracture surfaces exhibit surface or near-subsurface initiation sites, highlighted by red regions, and ductile overload areas, highlighted by the yellow regions. The wrought material shows one clear initiation region, akin to a more widely recognised mode of crack growth, whereas the LB-PBF variants exhibit more non-uniformity and multiple zones of crack nucleation. Despite this, it is not envisaged that the multiple crack initiation regions in the LB-PBF materials are associated with any process-induced defects given the volume fraction measurements recorded in Table 2 and the assumption that the materials are somewhat fully dense. Additional higher magnification images were also taken on the SEM (both SE and BSE) to highlight the initiation zones in more detail.

4. Conclusions

This study has comprehensively assessed the high-temperature performance of Laser Beam Powder Bed Fusion (LB-PBF) Inconel 718 (IN718) subjected to two distinct post-manufacture heat treatments, in comparison with both as-received (AR) LB-PBF and conventionally wrought material. The following conclusions can be drawn:

- Heat Treatment 1 (HT1) effectively refined the LB-PBF microstructure, increasing twin density and promoting a fine, well-dispersed distribution of strengthening precipitates (γ', γ'', δ, and carbides), contributing to superior mechanical performance. HT2, although also enhancing precipitate formation, resulted in coarser grain structures and a less optimal phase distribution.
- Both heat-treated LB-PBF variants (HT1 and HT2) significantly outperformed the AR material and wrought IN718 in terms of tensile strength at 650 °C, with HT1 offering a marginal advantage. However, this came at the expense of reduced ductility compared to the wrought material.
- All material variants exhibited evidence of dynamic strain aging (DSA) at 650 °C, though the magnitude and type varied. Wrought IN718 showed more regular and severe DSA features (Types B/C), while LB-PBF materials displayed more irregular (Types D/E) behaviour, indicative of microstructural heterogeneity.
- HT1 demonstrated creep resistance comparable to the wrought alloy, due to the synergistic effect of fine grain boundary strengthening precipitates and an intermediate grain size. In contrast, HT2 and AR materials exhibited inferior creep behaviour, with faster creep rates and reduced rupture lives.
- HT1 displayed the highest LCF performance among all tested variants, followed by HT2 and AR, with the wrought material exhibiting the lowest fatigue strength under cyclic loading at elevated temperature. This was attributed to the tailored precipitate structure and grain refinement from HT1.
- Fractographic analysis revealed that the wrought material retained the most ductile failure modes, with pronounced dimpling and necking. The LB-PBF variants, particularly HT1, showed more brittle features but benefited from multiple crack initiation resistance and uniform phase distribution.
- HT1 emerges as the optimal heat treatment for enhancing both fatigue and creep properties of LB-PBF IN718, offering mechanical performance closely aligned with or surpassing wrought material in high-temperature applications. The study confirms that post-processing plays a critical role in realising the full potential of additively manufactured superalloys for demanding service environments.

Data availability

The raw/processed data required to reproduce these findings cannot be shared at this time as the data also forms part of an ongoing study.

Declaration of competing interest

The authors declare that they have no known competing financial interests or personal relationships that could have appeared to influence the work reported in this paper.

Acknowledgements

The current research was funded under the EPSRC Industrial Case Award EP/T517987/1. The provisions of research bursary, materials, and supporting information from ASTM AMCoE is gratefully acknowledged. Mechanical tests were performed at Swansea Materials Research and Testing Ltd. (SMaRT). Utilisation of the FEG-SEM was provided by Swansea University's Faculty of Science & Engineering Advanced Imaging of Materials (AIM) Facility, which was funded in part by the EPSRC (EP/M028267/1), The European Regional Development Fund through the Welsh Government (80708) and the Ser Solar project via the Welsh Government.

References

[1] Attaran M. The rise of 3-D printing: the advantages of additive manufacturing over traditional manufacturing. Bus Horiz 2017;60:677–88. https://doi.org/10.1016/J.BUSHOR.2017.05.011.

[2] Bhatia A, Sehgal AK. Additive manufacturing materials, methods and applications: a review. Mater Today Proc 2023;81:1060–7. https://doi.org/10.1016/J.MATPR.2021.04.379.

[3] Kanishka K, Acherjee B. Revolutionizing manufacturing: a comprehensive overview of additive manufacturing processes, materials, developments, and challenges. J Manuf Process 2023;107:574–619. https://doi.org/10.1016/J.JMAPRO.2023.10.024.

[4] Irrinki H, Nath SD, Akilan AA, Atre SV. Laser powder bed fusion. In: Bourell D, Frazier W, Kuhn H, Seifi M, editors. Additive manufacturing processes, 24. ASM International; 2020. p. 209–19. https://doi.org/10.31399/asm.hb.v24.a0006621.

[5] Fidan I, Huseynov O, Ali MA, Alkunte S, Rajeshirke M, Gupta A, et al. Recent inventions in additive manufacturing: holistic review. Inventions 2023;8:103. https://doi.org/10.3390/INVENTIONS8040103. 2023;8.

[6] Sanchez S, Smith P, Xu Z, Gaspard G, Hyde CJ, Wits WW, et al. Powder Bed Fusion of nickel-based superalloys: a review. Int J Mach Tool Manufact 2021;165. https://doi.org/10.1016/J.IJMACHTOOLS.2021.103729.

[7] Getachew MT, Shiferaw MZ, Ayele BS. The current state of the art and advancements, challenges, and future of additive manufacturing in aerospace applications. Adv Mater Sci Eng 2023. https://doi.org/10.1155/2023/8817006.

[8] White M, Dobbs J. Additive manufacturing applications in aviation. Additive manufacturing design and applications. ASM International; 2023. p. 429–37. https://doi.org/10.31399/asm.hb.v24A.a0006989.

[9] Zhao N, Parthasarathy M, Patil S, Coates D, Myers K, Zhu H, et al. Direct additive manufacturing of metal parts for automotive applications. J Manuf Syst 2023;68:368–75. https://doi.org/10.1016/J.JMSY.2023.04.008.

[10] Kumar R, Kumar M, Chohan JS. The role of additive manufacturing for biomedical applications: a critical review. J Manuf Process 2021;64:828–50. https://doi.org/10.1016/J.JMAPRO.2021.02.022.

[11] Sun C, Wang Y, McMurtrey MD, Jerred ND, Liou F, Li J. Additive manufacturing for energy: a review. Appl Energy 2021;282:116041. https://doi.org/10.1016/J.APENERGY.2020.116041.

[12] Schoofs F, Garcia F, Geisen O. Additive manufacturing in the nuclear and wind energy sectors. Additive manufacturing design and applications. ASM International; 2023. p. 509–14. https://doi.org/10.31399/asm.hb.v24A.a0007019.

[13] DebRoy T, Wei HL, Zuback JS, Mukherjee T, Elmer JW, Milewski JO, et al. Additive manufacturing of metallic components – process, structure and properties. Prog Mater Sci 2018;92:112–224. https://doi.org/10.1016/j.pmatsci.2017.10.001.

[14] Mostafaei A, Ghiaasiaan R, Ho IT, Strayer S, Chang KC, Shamsaei N, et al. Additive manufacturing of nickel-based superalloys: a state-of-the-art review on process-structure-defect-property relationship. Prog Mater Sci 2023;136. https://doi.org/10.1016/J.PMATSCI.2023.101108.

[15] Gu D, Shi X, Poprawe R, Bourell DL, Setchi R, Zhu J. Material-structure-performance integrated laser-metal additive manufacturing. Science 1979;2021:372. https://doi.org/10.1126/science.abg1487.

[16] Gockel J. Structure-properties relationships in metal additive manufacturing. Additive manufacturing design and applications. ASM International; 2023. p. 23–9. https://doi.org/10.31399/asm.hb.v24A.a0006990.

[17] Kirka M. Process-structure relationships in fusion metals additive manufacturing. Additive manufacturing design and applications. ASM International; 2023. p. 16–22. https://doi.org/10.31399/asm.hb.v24A.a0006977.

[18] Wu Y, Li C, Xia X, Liang H, Qi Q, Liu Y. Precipitate coarsening and its effects on the hot deformation behaviour of the recently developed y' strengthened superalloys. J Mater Sci Technol 2021;67:95–104.

[19] Qi H, Azer M, Ritter A. Studies of standard heat treatment effects on microstructure and mechanical properties of laser net shape manufactured INCONEL 718. The minerals, 40A. Metals & Materials Society and ASM International; 2009 2009. https://doi.org/10.1007/s11661-009-9949-3.

[20] Gudivada G, Pandey AK. Recent developments in nickel-based superalloys for gas turbine applications: review. J Alloys Compd 2023;963. https://doi.org/10.1016/J.JALLCOM.2023.171128.

[21] Yong CK, Gibbons GJ, Wong CC, West G. A critical review of the material characteristics of additive manufactured IN718 for high-temperature application. Metals 2020;10. https://doi.org/10.3390/MET10121576.

[22] Pratheesh Kumar S, Elangovan S, Mohanraj R, Ramakrishna JR. A review on properties of Inconel 625 and Inconel 718 fabricated using direct energy deposition. Mater Today Proc 2021;46:7892–906. https://doi.org/10.1016/J.MATPR.2021.02.566.

[23] Hosseini E, Popovich VA. A review of mechanical properties of additively manufactured Inconel 718. Addit Manuf 2019;30:100877. https://doi.org/10.1016/J.ADDMA.2019.100877.

[24] Pollock TM, Tin S. Nickel-based superalloys for advanced turbine engines: chemistry, microstructure and properties. J Propul Power 2006;22:361–74. https://doi.org/10.2514/1.18239.

[25] Durand-Charre M. The microstructure of superalloys. Routledge; 2017. https://doi.org/10.1201/9780203736388.

[26] Lee GH, Park M, Kim B, Jeon JB, Noh S, Kim BJ. Evaluation of precipitation phase and mechanical properties according to aging heat treatment temperature of Inconel 718. J Mater Res Technol 2023;27:4157–68. https://doi.org/10.1016/j.jmrt.2023.10.196.

[27] Cozar R, Pineau A. Morphology of y' and y" precipitates and thermal stability of inconel 718 type alloys. Metall Trans A 1973;4:47–59. https://doi.org/10.1007/BF02649604.

[28] Shahwaz Md, Nath P, Sen I. A critical review on the microstructure and mechanical properties correlation of additively manufactured nickel-based superalloys. J Alloys Compd 2022;907. https://doi.org/10.1016/j.jallcom.2022.164530.

[29] Knorovsky GA, Cieslak MJ, Headley TJ, Romig AD, Hammetter WF. Inconel 718: a solidification diagram. Metall Trans A 1989;20:2149–58. https://doi.org/10.1007/BF02650300.

[30] Ma T, Zhang G-P, Tan P, Zhang B. Effects of homogenization temperature on creep performance of laser powder bed fusion-fabricated Inconel 718 at 650°C. Mater Sci Eng, A 2022;853. https://doi.org/10.1016/j.msea.2022.143794.

[31] Franco-Correa JC, Martínez-Franco E, Alvarado-Orozco JM, Cáceres-Díaz LA, Espinosa-Arbelaez DG, Villada JA. Effect of conventional heat treatments on the microstructure and microhardness of IN718 obtained by wrought and additive manufacturing. J Mater Eng Perform 2021;30:7035–45. https://doi.org/10.1007/s11665-021-06138-9.

[32] Meng G, Gong Y, Zhang J, Zhao J. Effect of heat treatment on microstructure, precipitation behavior and mechanical properties of Inconel 718 fabricated by laser direct energy deposition. Mater Sci Eng 2024;898. https://doi.org/10.1016/j.msea.2024.146396.

[33] Mostafa A, Rubio IP, Brailovski V, Jahazi M, Medraj M. Structure, texture and phases in 3D printed IN718 alloy subjected to homogenization and HIP treatments. Metals 2017. https://doi.org/10.3390/met7060196.

[34] Yu CH, Peng RL, Lee TL, Luzin V, Lundgren JE, Moverare J. Anisotropic behaviours of LPBF Hastelloy X under slow strain rate tensile testing at elevated temperature. Mater Sci Eng, A 2022;844:143174. https://doi.org/10.1016/J.MSEA.2022.143174.

[35] Popovich VA, Borisov EV, Popovich AA, Sufiiarov VS, Masaylo DV, Alzina L. Functionally graded Inconel 718 processed by additive manufacturing: crystallographic texture, anisotropy of microstructure and mechanical properties. Mater Des 2017;114:441–9. https://doi.org/10.1016/J.MATDES.2016.10.075.

[36] Ghorbanpour S, Sahu S, Deshmukh K, Borisov E, Riemslag T, Reinton E, et al. Effect of microstructure induced anisotropy on fatigue behaviour of functionally graded Inconel 718 fabricated by additive manufacturing. Mater Char 2021;179:111350. https://doi.org/10.1016/J.MATCHAR.2021.111350.

[37] Kumara C, Balachandramurthi AR, Goel S, Hanning F, Moverare J. Toward a better understanding of phase transformations in additive manufacturing of Alloy 718. Materialia 2020;13. https://doi.org/10.1016/j.mtla.2020.100862.

[38] Singh VK, Sahoo D, Amirthalingam M, Karagadde S, Mishra SK. Dissolution of the Laves phase and δ-precipitate formation mechanism in additively manufactured Inconel 718 during post printing heat treatments. Addit Manuf 2024;81. https://doi.org/10.1016/J.ADDMA.2024.104021.

[39] Ghorbanpour S, Deshmukh K, Sahu S, Riemslag T, Reinton E, Borisov E, et al. Additive manufacturing of functionally graded inconel 718: effect of heat treatment and building orientation on microstructure and fatigue behaviour. J Mater Process Technol 2022;306. https://doi.org/10.1016/j.jmatprotec.2022.117573.

[40] Doğu MN, Davut K, Obeidi MA, Yalçın MA, Gu H, Low TSE, et al. Recrystallization and grain growth kinetics of IN718 manufactured by laser powder bed fusion. J Mater Res Technol 2022;19:4242–57. https://doi.org/10.1016/j.jmrt.2022.06.157.

[41] Popovich VA, Borisov EV, Popovich AA, Sufiiarov VSh, Masaylo DV, Alzina L. Impact of heat treatment on mechanical behaviour of Inconel 718 processed with tailored microstructure by selective laser melting. Mater Des 2017;131:12–22. https://doi.org/10.1016/j.matdes.2017.05.065.

[42] Ni M, Chen C, Wang X, Wang P, Li R, Zhang X, et al. Anisotropic tensile behavior of in situ precipitation strengthened Inconel 718 fabricated by additive manufacturing. Mater Sci Eng, A 2017;701:344–51. https://doi.org/10.1016/j.msea.2017.06.098.

[43] Li Z, Lin X, Sui S, Zhao X, Yao B, Zhong C, et al. Single-crystal structure formation in laser directed energy deposited Inconel 718 through process parameter optimization and substrate orientation tuning. J Mater Process Technol 2025;335. https://doi.org/10.1016/j.jmatprotec.2024.118673.

[44] Wang Y, Guo W, Xu C, Zhang Y, Ji Q, Feng X, et al. Defects, microstructure, and properties in laser powder bed fusion IN718: power density effects and feature maps. J Manuf Process 2025;135:240–52. https://doi.org/10.1016/j.jmapro.2025.01.054.

[45] Liu H, Cheng W, Sun Y, Ma R, Wang Y, Bai J, et al. Effects of process parameters and heat treatment on microstructure and mechanical characteristics of laser powder bed fusion alloy inconel 718. Coatings (Oakv) 2023;13. https://doi.org/10.3390/coatings13010189.

[46] Kasperovich G, Gussone J, Requena G, Schell N, Stark A, Haubrich J. Tailoring the strength of inconel 718: insights into LPBF parameters and heat treatment synergy. Mater Des 2025;250. https://doi.org/10.1016/j.matdes.2025.113627.

[47] BSI. BS ISO 13067:2020 Microbeam analysis. Electron backscatter diffraction. Measurement of average grain size; 2020.

[48] ASTM International. ASTM E92-12 standard test methods for Vickers hardness and knoop hardness of metallic materials. Book of Standards 2023:1–28. https://doi.org/10.1520/E0092-23.

[49] ASTM International. ASTM E8/E8M-21: standard test methods for tension testing of metallic materials. 2022.

[50] ASTM International. ASTM E139-11: standard test methods for conducting creep, creep-rupture, and stress-rupture tests of metallic materials, vols. 1–14; 2018.

[51] BSI Standards Publication. BS ISO 12106: metallic materials - fatigue testing - axial-strain-controlled method. 2017. p. 1–38.

[52] Zhang RY, Qin HL, Bi ZN, Li J, Paul S, Lee TL, et al. Evolution of lattice spacing of gamma double prime precipitates during aging of polycrystalline Ni-base superalloys: an in situ investigation. Metall Mater Trans 2020;51:574–85. https://doi.org/10.1007/s11661-019-05536-y.

[53] Ghaemifar S, Mirzadeh H. Precipitation kinetics of gamma double prime phase during direct aging treatment of Inconel 718 superalloy additively manufactured

by selective laser melting. J Mater Res Technol 2023;27:4248–55. https://doi.org/10.1016/j.jmrt.2023.10.267.
[54] Ferreri NC, Vogel SC, Knezevic M. Determining volume fractions of γ, γ′, γ″, δ, and MC-carbide phases in Inconel 718 as a function of its processing history using an advanced neutron diffraction procedure. Mater Sci Eng, A 2020;781. https://doi.org/10.1016/j.msea.2020.139228.
[55] Bryndza G, Tchuindjang JT, Chen F, Habraken AM, Sepúlveda H, Tuninetti V, et al. Review of the microstructural impact on creep mechanisms and performance for laser powder bed fusion inconel 718. Materials 2025;18. https://doi.org/10.3390/ma18020276.
[56] Desvallees Y, Bouzidi M, Bois F, Beaude N. Delta phase in INCONEL 718: mechanical properties and forging process requirements. Superalloys 718, 625, 706 and various derivatives (1994). TMS; 1994. p. 281–91. https://doi.org/10.7449/1994/Superalloys_1994_281_291.
[57] Rezende MC, Araújo LS, Gabriel SB, Dille J, de Almeida LH. Observations on dynamic strain aging manifestation in inconel 718 superalloy. Mater Sci Forum 2018;930:390–4. https://doi.org/10.4028/www.scientific.net/MSF.930.390.
[58] Saravanan K, Chakravadhanula VSK, Manwatkar SK, Narayana Murty SVS, Ramesh Narayanan P. Dynamic strain aging and embrittlement behavior of IN718 during high-temperature deformation. Metall Mater Trans 2020;51A:5691–703. https://doi.org/10.1007/s11661-020-05970-3.
[59] Weaver ML, Hale CS. Effects of precipitation on serrated yielding in inconel 718 . Superalloys 718, 625, 706 and various. Derivatives 2001:421–32.
[60] Gao M, Wei RP. Grain boundary niobium carbides in inconel 718. Scr Mater 1997;37:1843–9. https://doi.org/10.1016/S1359-6462(97)00373-4.
[61] Zhang S, Weng K, Guo C, Zhao H, Lin X, Wang L, et al. The creep behavior of IN718 alloy fabricated by selective laser melting compared to forging. Appl Mater Today 2024;38. https://doi.org/10.1016/j.apmt.2024.102252.
[62] Kuo Y-L, Kamigaichi A, Kakehi K. Characterization of Ni-based superalloy built by selective laser melting and Electron beam melting. Metall Mater Trans 2018;49:3831–7. https://doi.org/10.1007/s11661-018-4769-y.
[63] Oros TJ, Son K, Hodge AM, Kassner ME. The high temperature creep and fracture behavior of Inconel 718 produced by additive manufacturing. Scr Mater 2024;251. https://doi.org/10.1016/j.scriptamat.2024.116208.
[64] Sonntag N, Piesker B, Ávila Calderón LA, Mohr G, Rehmer B, Agudo Jácome L, et al. Tensile and low-cycle fatigue behavior of laser powder bed fused inconel 718 at room and high temperature. Adv Eng Mater 2024;26. https://doi.org/10.1002/adem.202302122.
[65] Song Z, Gao W, Wang D, Wu Z, Yan M, Huang L, et al. Very-high-cycle fatigue behavior of inconel 718 alloy fabricated by selective laser melting at elevated temperature. Materials 2021;14:1001. https://doi.org/10.3390/ma14041001.
[66] Nezhadfar PD, Johnson AS, Shamsaei N. Fatigue behavior and microstructural evolution of additively manufactured Inconel 718 under cyclic loading at elevated temperature. Int J Fatig 2020;136:105598. https://doi.org/10.1016/j.ijfatigue.2020.105598.